Design of a Lightweight and Deployable Soft Robotic Arm

robotics

MDPI

Article

Design of a Lightweight and Deployable Soft Robotic Arm

Pierpaolo Palmieri *, Matteo Melchiorre and Stefano Mauro

Department of Mechanical and Aerospace Engineering, Politecnico di Torino, 10129 Turin, Italy
* Correspondence: pierpaolo.palmieri@polito.it

Abstract: Soft robotics represents a rising trend in recent years, due to the ability to work in unstructured environments or in strict contact with humans. Introducing soft parts, robots can adapt to various contexts overcoming limits relative to the rigid structure of traditional ones. Main issues of soft robotics systems concern the relatively low force exertion and control complexity. Moreover, several fields of application, as space industry, need to develop novel lightweight and deployable robotic systems, that can be stored into a relatively small volume and deployed when required. In this paper, POPUP robot is introduced: a soft manipulator having inflatable links and rigid joints. Its hybrid structure aims to match the advantages of rigid robots and the useful properties of having a lightweight and deployable parts, ensuring simple control, low energy consumption and low compressed gas requirement. The first robot prototype and the system architecture are described highlighting design criteria and effect of internal pressure on the performances. A pseudo-rigid body model is used to describe the behavior of inflatable links looking forward to control design. Finally, the model is extended to the whole robot: multi-body simulations are performed to highlight the importance of suitable sensor equipment for control development, proposing a visual servoing solution.

Keywords: soft robotics; space robotics; flexible robotics; dynamic modeling; inflatable structures

Citation: Palmieri, P.; Melchiorre, M.; Mauro, S. Design of a Lightweight and Deployable Soft Robotic Arm. *Robotics* **2022**, *11*, 88. https://doi.org/10.3390/robotics11050088

Academic Editors: Inderjeet Singh and Paolo Mercorelli

Received: 13 August 2022
Accepted: 29 August 2022
Published: 31 August 2022

1. Introduction

Over the last few years, robots with soft bodies [1] have captured significant interest and represent a growing trend. Soft robotics allows the design and development of complex systems able to adapt unstructured and hostile environment [2]. They offer important advantages in several tasks, ranging from search and exploration missions [3] to the cooperation with humans [4]. Soft robots are typically divided in two categories: articulated [5] and continuum ones [6], and their design is often inspired by biological systems [7]. Additionally, soft robots can span along all the spectrum between totally soft [8] and rigid structures [9].

Inflatable structures have been applied in the field of soft robotics because of their lightweight and physical compliance increasing payload-to-weight ratio. Moreover, their construction tends to reduce costs if compared with other lightweight solutions [10]. Main disadvantages of these systems are low payload capacity, due to the actuation system and low stiffness, and complexity in kinematics and dynamics description [11], due to non-linearities induced by large deformations in the material and multi-physical coupling.

Robots with rigid structures are employed in space environments, for on-board [12] and off-board [13] applications, executing tasks with great accuracy and generating high contact forces. Moreover, robots for space environments must be properly designed to satisfy strict requirements, such as weight and embarked volume. In space environments, deploying strategies mainly consist in mechanisms with interconnected bar elements [14], or inflatable structure with pressure input [15]. This second solution has been successfully used in space applications, where some of the most relevant projects are: the Inflatable Antenna Experiment (IAE) [16], the inflatable and rigidable solar array [17] and modular inflatable membranes of James Webb Space Telescope [18].

In literature, soft robots can be described with approaches based on constant [19] and non-constant curvature approximation [20]. However, manipulators with inflatable links can be modeled considering traditional approaches developed for flexible link arms [21], pseudo-rigid body models [22] and simplified small deflection assumptions [10]. The use of algorithms for the robot dynamic parameters identification, as shown in [23], allows us to obtain a full dynamic description of manipulators, also considering the effects of temperature and mounting configuration [24]. In soft robotics, several control approaches have been proposed. In [25], a pressure control system has been used to perform the characterization of a soft joint for inflatable robotic arms (IRAs), actuated by two antagonist pneumatic artificial muscles (PAMs). In [26], a pneumatically actuated humanoid robot, with two IRAs, is controlled using model predictive control (MPC) and linear quadratic regulation (LQR) in the joint space and in [27] the MPC is compared against sliding mode control (SMC). In [28], fuzzy logic allows a precise control of pneumatic actuated robots. Moreover, many control methods for soft robots are based on machine learning techniques, e.g., in [29], where a neural network is used to control a cable-driven soft arm. Deep learning can lead to the development of visual servoing (VS) systems [30]. Vision systems, widely used in robotics, can be especially useful for soft robots. In [31], VS is used to have accurate shape control of a cable-driven soft manipulator, and in [32] a vision-based controller is applied to soft robots to execute tasks without prior knowledge of system parameters. In [33], SMC based on image processing algorithms is used to calculate real time path of robot motion.

When robots share the workspace with humans, the risk of an undesired collision during their operation must be minimized. Recently, the use of vision systems [34,35] with state estimators [36] and collision avoidance algorithms [37] using data from multiple sensors [38] has enhanced human–robot collaboration (HRC) [39]. However, robots with intrinsic soft structure and contact detection algorithms [40] can improve safety, since the soft structure has the effect of absorbing energy during an undesired impacts [41]. Furthermore, users perceive soft robots safer than traditional ones [42].

This paper discloses the prototype of POPUP, a deployable and lightweight robotic arm, consisting in inflatable links and rigid electric-actuated joints. It includes build-in sensors to enhance and facilitate the system control. It can be stored in a relative small package and deployed when required, guaranteeing weight and volume savings. This feature is relevant for space applications, where it leads to reduced costs. The prototype has been developed after considerations from previous works, where preliminary control strategies [43] have been investigated. Two different applications are considered: a first one dedicated to open space missions, in which a large robotic harm is needed for debris capture or berthing operation [44], and onboard application, where a soft collaborative robot can help the crew in its tasks [45].

The link of the prototype has been statically and dynamically characterized by using a pseudo-rigid body model (PRBM). The model is extended to the whole robot, allowing to account link deflections with the use of virtual joints. The proposed model is light and easily manageable from a control point of view, with respect to alternatives as assumed mode method (AMM) [21] and finite element method (FEM) [46]. As a matter of fact, since the purpose is providing a dynamic model that can be used for the development of control algorithms and capable of effectively considering link deflections, the PRBM is a great trade-off in terms of lightness, accuracy and flexibility.

Using the dynamic model of the robot that considers link deflections, a task of target reaching has been simulated with different control strategies. At first, the robot has been controlled as rigid, underlining the impact of link deflections on positioning performances. Finally, a solution based on visual servoing has been proposed, showing the feasibility of this control approach to compensate link deflections and correctly reach the target.

This work puts the basis for the development and testing of control algorithms on the POPUP robot prototype.

2. Project Objectives

The project purpose is the development of a robotic manipulator with large inflatable links for space applications. The robot architecture is intended to be comparable to other space robotic manipulator, e.g., Canadarm [47], having two links longer than the other ones, and able to reach 6 degrees of freedom (DOF) or more adding suitable joints. This concept is based on the idea of having the two long links inflatable, since they represent the majority of volume occupied by the robot. Robots with inflatable links lead to a cost-effective solution for space missions, because of weight and volume savings.

In contrast with other inflatable robotic arms with pneumatic actuation, the use of traditional electric motors allows us to have simpler control and lower size of the pneumatic line. For POPUP robot, link inflation and deflation are an ON/OFF process with simple pneumatic control. Moreover, several inflation cycles can be performed. The air supply can be provided by a pressurized tank in composite materials having limited dimensions with respect to the robot. As an example, the dimensions of the first version of Canadarm robot embedded on the Space Shuttle [47], indicated in the following as Canadarm1, are taken as reference: assuming link length of 6 m, link radius of 165 mm, inner pressure of 100 kPa and tank pressure of 30 MPa, the tank volume per inflation cycle is 4 dm^3, that is, less than 0.4% of total robot volume. Finally, advantages in terms of volume savings grow with the increase of ratio of link lengths to joint sizes. For example, assuming a reduction of 75% of link volume when deflated, the overall volume savings would be of 60% for a POPUP with the structure of a Canadarm1, reducing the volume from 1.3 m^3 to 0.5 m^3.

The design parameter for link dimensioning is the wrinkling moment, that is, the bending load for which the first wrinkles appear on the link, resulting in non-linear behavior of the inflatable beam. Theoretically, the wrinkling moment M_w is half the collapse moment M_c, that is, the bending load for which an increase in deflection does not correspond to an increase in reaction force [48]. The following semi-empirical formula [49] is considered to define the collapse moment:

$$M_c = \frac{\pi^2}{4} p r^3, \tag{1}$$

where p is the relative inner pressure, and r is the radius of the link. This formulation allows preliminary analysis about dimensions, payload and pressure used during the operative stage of the robot when deployed. As an example, taking again as reference the Canadarm1 dimensions, assuming inner pressure of 100 kPa and neglecting robot inertia, POPUP could support 40 N of load applied on the end-effector (EE) without showing wrinkles, that means moving a payload of 400 kg at 0.1 m/s^2 in the space. Since inner pressure is proportional to the achievable payload, it can be properly tuned according to the application.

A prototype of POPUP has been developed to study control strategies and examine suitable sensors. In this phase, materials are not purpose of the study. Final version expects to have a structural layer providing air insulation and load bearing, composed by a bladder and a webbing, and a protection layer for micrometeoroids and orbital debris (MMOD), abrasion, radiation and thermal defense.

Experiments are performed in presence of gravity. This aspect adds complications for the development of robot control. Nevertheless, effect of gravity can be easily decoupled in dynamic simulations. In addition, robustness of control algorithms is strengthen by the presence of deflections due to gravity, that can be seen as intensification of static hysteresis or misalignment phenomena in zero gravity environment.

3. System Design

POPUP robot prototype, shown in Figure 1, consists in a deployable robot with hybrid structure consisting of two inflatable links, three electric motors and rigid joints made by additive manufacturing.

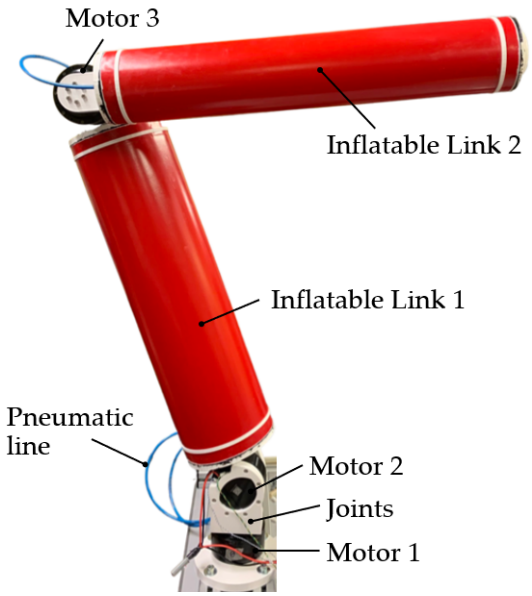

Figure 1. POPUP robot prototype: inflatable links, rigid joints, electric motors and pneumatic line.

The system includes a pneumatic line for the inflation of the links, an electronic circuit and built-in sensors. The EE presents a flange to easily permit the assembly a robotic wrist and/or a generic tool, increasing the DOF of the robot. Therefore, the robotic arm has 3 DOF, in its basic form, that can be extended depending on the application.

3.1. Mechanical Design

The robot links have cylindrical shape. The cylindrical surface is made by wounding a sheet of polymeric material. On the extremities two rigid rings are glued. The rings permit the links to be fixed through screws to the other joints, as shown in Figure 2, allowing the possibility to add elements, e.g., sensors, inside the links during development stages. The motor joints represent the link tops and guarantee their isolation by using seals.

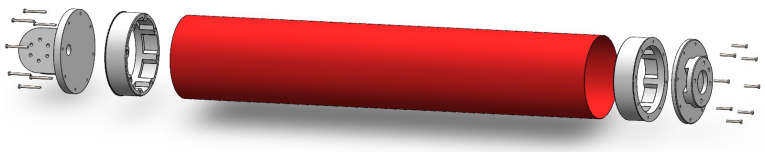

Figure 2. Exploded view drawing of POPUP link 2 prototype.

Both links have length $L = 600$ mm, link 1 has radius $r_1 = 85$ mm and link 2 has radius $r_2 = 55$ mm. Dimensions have been calculated using the wrinkling moment M_w formulation derived by Equation (1) in order to reach a payload of 20 N, without showing wrinkles, at a pressure of 60 kPa. Since robot links have been successfully tested in the range 10–90 kPa, the prototype payload can reach 30 N. The motors of the joints are brushless, with 80:1 reduction ratio, having a radius of 49 mm, a thickness of 62 mm and, mass of about 0.8 kg each, rated torque of 48 Nm and peak torque of 144 Nm. Since the biggest contribution to the mass is due to the motors, the robot mass is under 4 kg. The mass account does not consider power supply generators or the tank, since not yet available as ad-hoc allocation.

3.2. Pneumatic Line and Deployment

The system architecture is shown in Figure 3 where the pneumatic line and the electronic circuit are schematized.

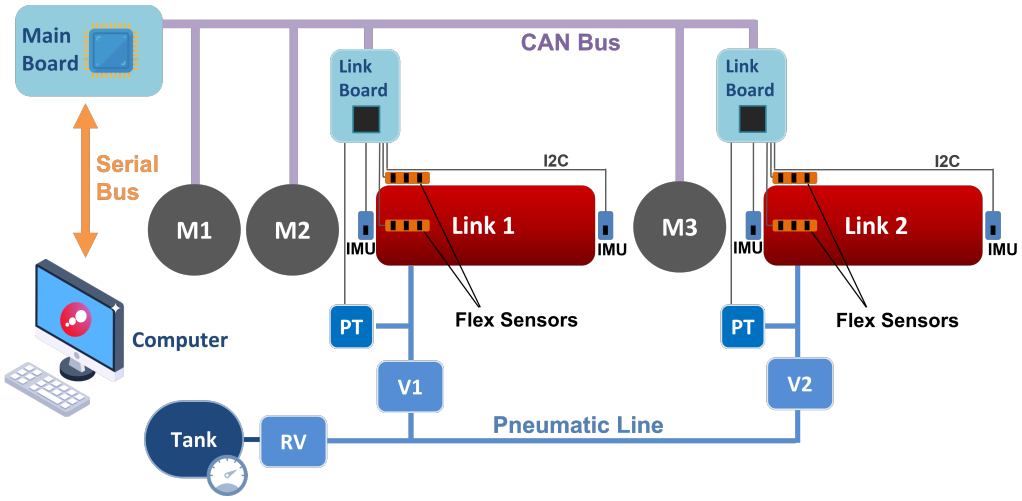

Figure 3. System architecture scheme: motors (M), links, inertial measurements units (IMUs), flex sensors, pneumatic line, main and link boards, computer.

A pneumatic line is responsible for the inflation and deflation of the links. Pressure supply is regulated by a reducing valve (RV) that provides pressure in the tested working range of 10–90 kPa. The links show acceptable performances with a pressure starting from 10 kPa. Internal pressure is measured through pressure transducers (PTs) mounted in proximity of the links. Compressed air can be provided by a pressurized tank or external pneumatic plant. Two valve groups, V1 and V2 for link 1 and 2 respectively, can provide pressure or deflate each the link separately. Valve groups consists of two digital valves: one connects the link with supply and the other one empties it. Valves are normally closed to avoid waste of energy, since they are activated only for inflation and deflation stages.

Links can be independently inflated and deflated to optimise the control of the deployment procedure. Once deployed and reached the working configuration, the pneumatic supply can be cut-off, although a by-pass should be considered to overcome air losses and maintaining constant the internal pressure. The tank, pressurized at 30 MPa and having a volume of 2 dm^3, allows us to inflate both links at a pressure of 50 kPa more than 10 times.

A demonstration of the deployment stage has been performed and shown in Figure 4.

In the deflated configuration the robot could be potentially contained in a box, having a volume of $0.3 \times 0.3 \times 0.4$ m against the operational working space of the extended robot of 1.4 m of radius if approximated with a sphere. The deployment stage includes different phases that facilitate the correct positioning and stability of the robot. For first, link 1 has been inflated and when the PT indicates it has reached the desired internal pressure, link 2 has been inflated to conclude the deployment. Built-in sensors are included to provide feedback about the success of the operation. In the current prototype, after the deflation, robot packing is assisted by user. A version with automatic wrapping is under development and described in [44].

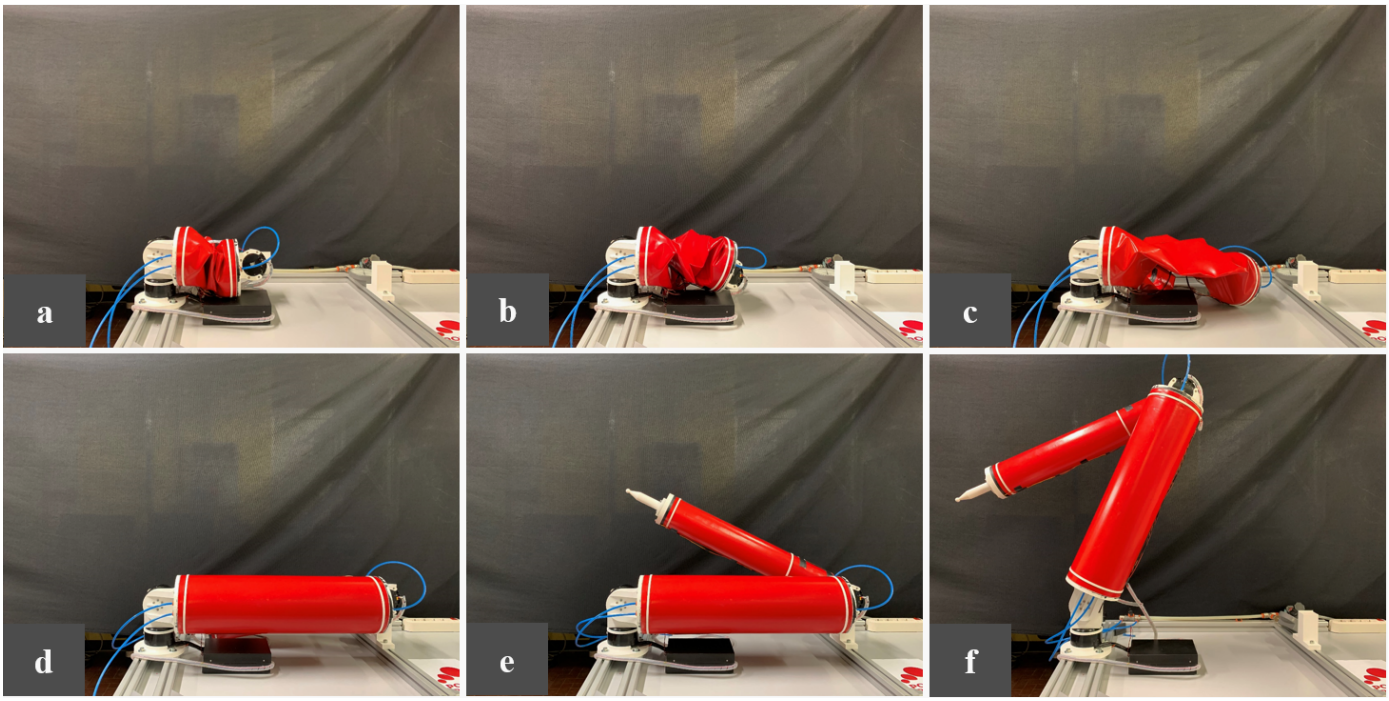

Figure 4. Deployment stage of the POPUP robot prototype. Deflated configuration (**a**), start of the inflation of link 1 (**b**), continuation of the inflation (**c**), inflation of link 1 completed and start of inflation od the link 2 (**d**), links inflated and stabilizing (**e**), robot deflated and in working configuration (**f**).

3.3. Sensors and Control Strategy Concept

Each link is equipped by sensors that provide an estimation of link deflections. Inertial measurement units (IMUs) are mounted on link extremities providing accelerations and absolute orientations by which the link deflections can be calculated. In addition, four flex sensors are positioned around the link cylinder region with higher static stress, i.e., the extremity closer to robot base in the kinematic chain. Each link is equipped by a dedicated board, called link board. Link boards acquire information from different transceivers and sensors, by I2C communication bus. A main board, responsible of the robot control, communicates with link boards and motors by CAN bus. A computer can be connected to the main board and manage robot tasks.

Sensor fusion and state estimation techniques, e.g., Kalman filter [50], using information by sensors, can be employed to better estimate actual link state to properly control the robot, reducing inaccuracies due to the non-linearities of the system. Measured deformations are useful to obtain a better estimate of EE position through direct kinematics and to monitor the link condition and detect the wrinkling state. Strategies aiming to avoid wrinkling can be implemented considering acceleration limitation. In addition, vibrations can be reduced using link acceleration data in the control law: joint accelerations can be actively limited and/or properly set such as to compensate link accelerations.

Furthermore, a depth camera can be mounted on EE to identify the target and performing grasping operations with an accuracy that does not depend on the link state estimation: the camera can evaluate a relative positioning error between EE and target, producing a velocity set with respect to EE, allowing target following. More complex camera systems can be evaluated, e.g., additional cameras can be positioned on base to develop advanced logic for robot state estimation and for target identification, following and grasping.

4. Inflatable Link Model and Experimental Tests

Each link is modeled as two rigid bodies connected by a virtual hinge with a torsional spring and dumper, as shown in Figure 5.

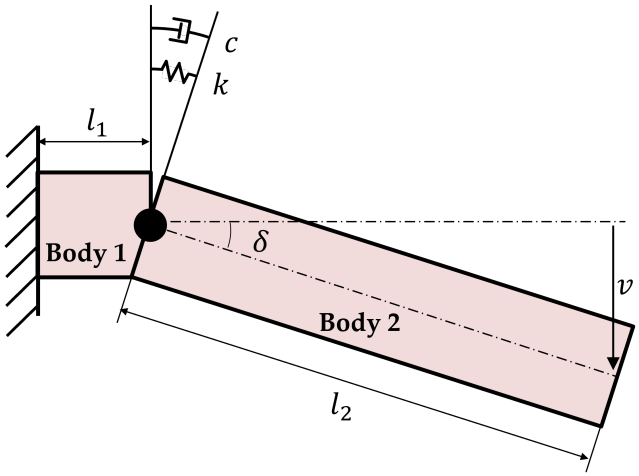

Figure 5. Pseudo-rigid body model of the link, considered as cantilever.

The link motion is described by the equation:

$$I\ddot{\delta} + c(p)\dot{\delta} + k(p)\delta = \tau, \tag{2}$$

where I is the moment of inertia, τ the external torque, δ the angular deflection, k and c respectively the stiffness and damping coefficients considered as depending on the internal pressure p. In addition, l_1 is the length of body 1, l_2 is the length of body 2 and v is the extremity displacement. This pseudo-rigid body model (PRBM) can be considered effective until the pressure is able to maintain the link walls taut, otherwise the formation of wrinkles leads to the collapse of the structure.

Experiments

Static and dynamic tests have been performed in order to analyse pressure effects on bending link response. The set-up is shown in Figure 6. A link prototype, having the same features of link 2, is mounted on a fixed joint to be treated as cantilever. The pressure supply value is regulated by a reducing valve and measured by a transducer. The static tests have been performed applying a known incremental load on the free link extremity to obtain the relations between load and displacement on varying the internal pressure. The dynamic tests have been carried out to evaluate the first damped natural frequencies f_s of the link in relation to the internal pressure, by measuring the power spectral density (PSD) and the frequency response function (FRF). Therefore, two accelerometers are placed on the link to record the free oscillations generated by an instrumented impact hammer.

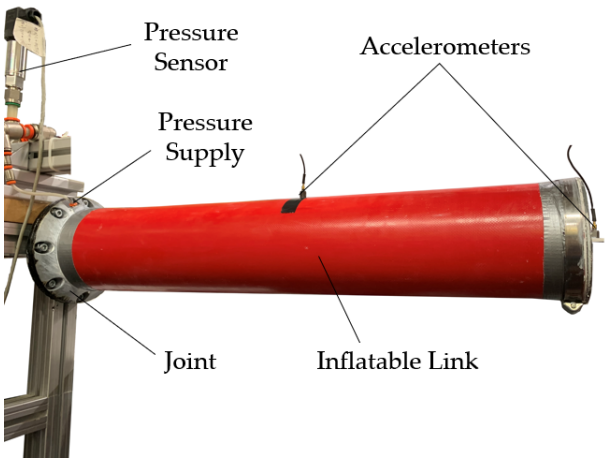

Figure 6. Experimental set-up of dynamic tests on the inflatable link prototype.

Static measurements have been converted in torque and angular deflection according the pseudo-rigid body model and having set $l_1 = 30$ mm and $l_2 = 570$ mm, considering the position where first winkles appear. In static tests, executed in the pressure range 10–50 kPa, a linear region has been found and a linear regression has been performed to calculate the stiffness coefficient k. The linear region can be identified using the wrinkling moment M_w as limit, since it reasonably fits the experimental evidences. From the dynamic tests, for each pressure level in the range 10–90 kPa, the damped natural frequency f_s has been reported and the damping ratio ζ has been evaluated using the logarithmic decrement method. In order to identify the moment of inertia associated to the virtual hinge in Figure 5, a recursive process has been implemented. Through the un-damped natural frequency and the stiffness coefficient k, the moment of inertia I has been estimated for each test. Then, the mean of the moments of inertia has been considered as a better estimate, since the value of the moment of inertia should be the same for each pressure level, neglecting the effect of an increase in mass due to an increase of the air pressure. Backwards, from moment of inertia and un-dumped natural frequencies, a coherent estimate of the stiffness coefficients $\widehat{k}$ has been calculated, adjusting the previous estimation, and extracting values for each pressure level of dynamic tests. Lastly, the damping coefficients $\widehat{c}$ have been evaluated, using the damping ratio ζ and moment of inertia. Results, shown in Table 1, highlight the dependence of stiffness and damping coefficient on pressure, that is, not directly proportional instead of wrinkling moment relation.

Table 1. Test results: estimated parameters.

p (kPa)	f_s (Hz)	$\widehat{c}$ (Nms/rad)	k (Nm/rad)	$\widehat{k}$ (Nm/rad)
10	15.04	0.557	296	321
20	15.63	0.547	346	347
30	15.94	0.463	348	360
40	16.17	0.450	389	370
50	16.44	0.433	407	382
60	16.56	0.429	N/A	388
70	16.65	0.412	N/A	392
80	16.83	0.407	N/A	401
90	16.93	0.406	N/A	405

Static tests have been improved performing both loading and unloading of the link in order to highlight the presence of hysteresis. Results are shown in Figure 7, where the averaged value of three measurements are reported. Results underline the dependence of link static characteristic on the internal pressure, confirming the significance of wrinkling moment M_w as limit value for linear region and collapse moment M_c as correct indicator for the maximum load acceptable, underlining its proportionality with pressure. As an example, the theoretical collapse moment at 30 kPa is calculated as $M_c = 12$ Nm by using Equation (1); this demonstrates the validity of the formulation as conservative design parameter. The maximum span of the hysteresis is about 0.5 deg, that is around 5 mm as extremity displacement of the link.

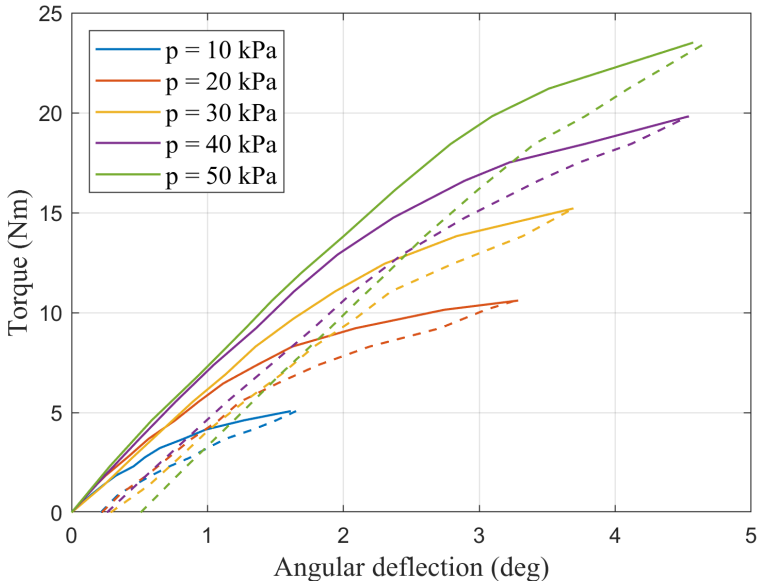

Figure 7. Static characteristic of the link prototype depending on the internal pressure level, averaged data based on 3 measures. Loading (solid line) and unloading (dashed line).

5. Robot Modeling and Simulation

Extending the link model to evaluate the deflections along two orthogonal axes and neglecting the torsional deformations, the robot kinematic chain reaches 7 DOF. This description adds virtual uncontrolled joint variables, indicated as $\delta_{i,j}$, where i is referred to the inflatable link number and j to the orientation. In Figure 8, the schemes of pseudo-rigid body model (PRBM) with flexible links and 7 DOF and the rigid body model (RBM) with 3 DOF are illustrated. Base frame, EE frame given the RBM and EE frame given the PRBM are represented. The Denavit–Hartenberg (D-H) parameters of the robot PRBM are shown in Table 2. Listed parameters refer to physical and virtual links that appear in the definition of the robot with virtual joints: for instance, virtual link 1.2 connects virtual joint $\delta_{1,2}$ with physical joint q_3.

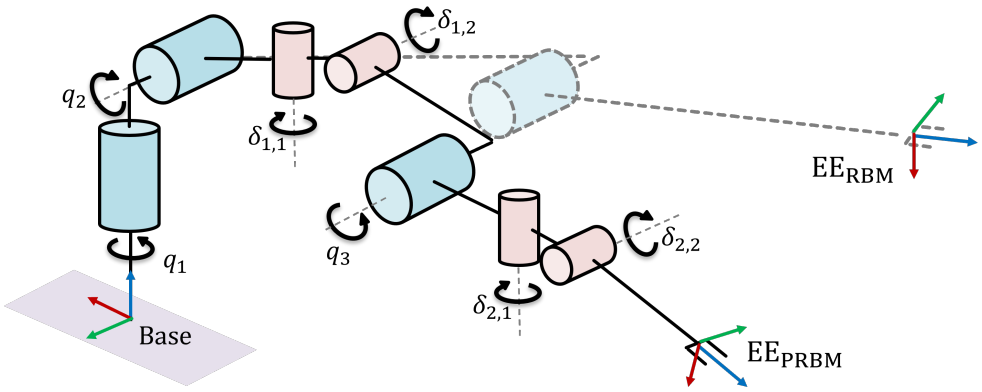

Figure 8. Robot kinematic scheme considering pseudo-rigid body model with virtual joints (PRBM, solid line) and rigid body model (RBM, dashed line).

Table 2. Prototype D-H parameters, PRBM with virtual joints.

Link	a_i (mm)	α_i (rad)	d_i (mm)	θ_i (rad)
0	0	$\pi/2$	152.70	q_1
1	94	$-\pi/2$	39.35	q_2
1.1	0	$\pi/2$	0	$\delta_{1,1}$
1.2	634	π	0	$\delta_{1,2}$
2	94	$\pi/2$	157.80	q_3
2.1	0	$-\pi/2$	0	$\delta_{2,1}$
2.2	590	0	0	$\delta_{2,2}$

A dynamic model of the robot with flexible links has been developed using the software Simscape Multibody™. In Figure 9, the POPUP robot rendering with PRBM is shown. Dynamic parameters have been set using values based on experimental tests previously discussed. The link 1 stiffness coefficients has been calculated from link 2 values, according to the well-known formulation used for lumped-parameter methods $k = EI_A/l$, with E the material Young's modulus, I_A the second moment of area and l the length of the beam unity, that is, l_2 in this specific case. Since link 1 differs from link 2 only for its cross-sectional area, the stiffness coefficients are scaled by the ratio of the second moments of area of the links. As a first approximation, the damping coefficient of link 1 has been estimated proportional to the stiffness coefficient. However, identification of robot dynamic parameters, executed using robot movements, is necessary to provide better accuracy to the system model. Hysteresis phenomena have been neglected. Alerts indicating a wrinkling condition have been implemented, monitoring virtual joint reaction torques.

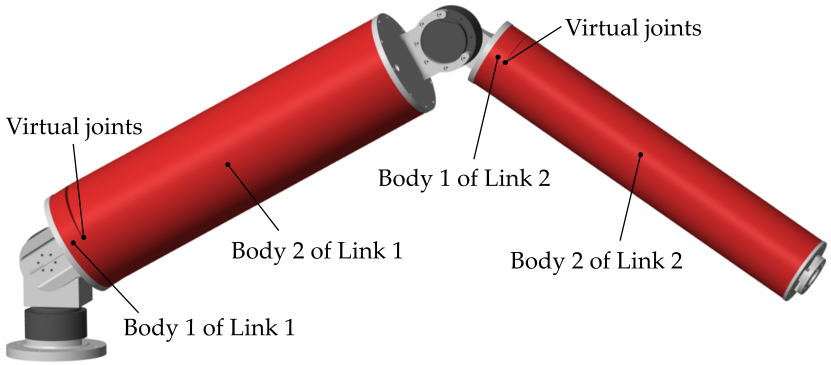

Figure 9. Graphic output of multi-body model.

A task, consisting in a target reaching, has been defined to underline main issues for the POPUP robot control. The target position $\boldsymbol{x}_d$ has been chosen to move the robot toward a more extended configuration, highlighting deflections due to the gravity. The robot control consists in a differential kinematics approach based on the Jacobian matrix $\boldsymbol{J}(\boldsymbol{q})$ of the rigid body model, with 3 DOF, that relates joint and EE velocities. A suitable choise for the desired velocity $\boldsymbol{v}_d(t)$ is:

$$\boldsymbol{v}_d(t) = min(a_0 t, v_0, (2a_0\|\boldsymbol{d}(t)\|)^{\frac{1}{2}})\frac{\boldsymbol{d}(t)}{\|\boldsymbol{d}(t)\|}, \tag{3}$$

where $\boldsymbol{d}(t) = \boldsymbol{x}_d - \boldsymbol{x}_e$ is the relative distance between target position $\boldsymbol{x}_d$ and EE position $\boldsymbol{x}_e$, a_0 is the maximal initial acceleration and v_0 is the maximal velocity. This approach allows us to have zero velocity at initial and final points, and it is suitable for other tasks, as following of a target in movement, e.g., space debris grasping. In Figure 10 a scheme of the simulated task is shown: the robot, represented in the starting configuration $\boldsymbol{q}_0 = [0, 60, -120]^T$ deg, has to reach the desired EE position $\boldsymbol{x}_d = [-800, 800, 400]^T$ mm in base frame. Yellow and green spheres highlight EE position $\boldsymbol{x}_e$ and target position $\boldsymbol{x}_d$ respectively.

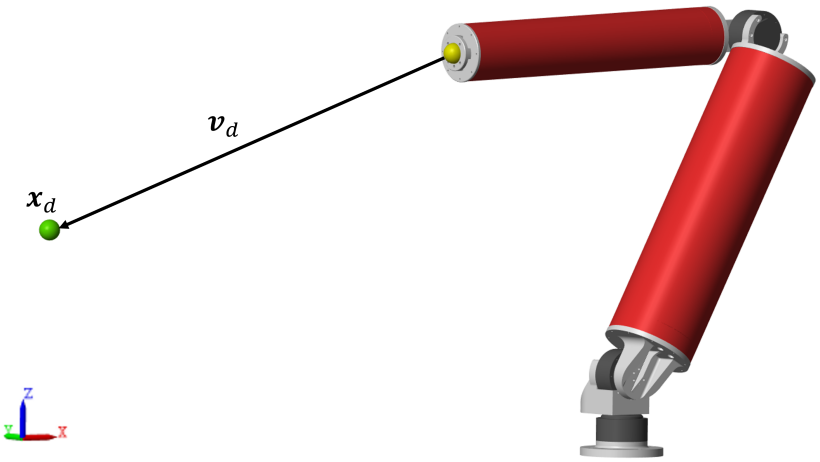

Figure 10. Scheme of the simulated task.

The following parameters have been set: payload of 2 kg, internal pressure $p = 60$ kPa, maximal velocity $v_0 = 0.1$m/s and maximal acceleration of $a_0 = 0.05$ m/s^2.

First simulation aims to underline differences in EE positioning between the flexible link robot and an equivalent rigid link robot, having same joint state. The virtual robot with flexible links has been controlled as a traditional rigid link robot, as shown in Figure 11.

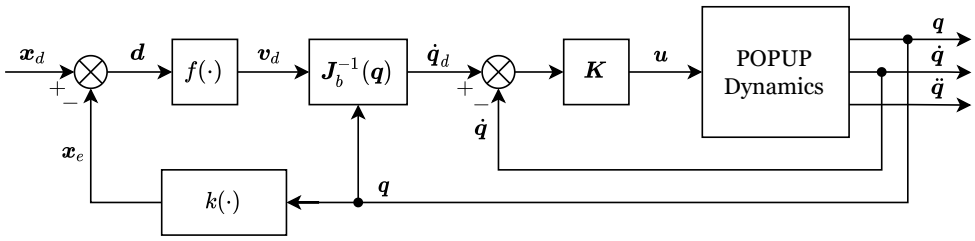

Figure 11. Block scheme of POPUP control using RBM.

EE position x_e is calculated by direct kinematics $k(\cdot)$ of RBM and expressed in base frame, function $f(\cdot)$ represents Equation (3), $J_b(q)$ is the Jacobian matrix of RBM in base frame, $\dot{q}_d$ is the desired joint velocity, K is the matrix gain, u is the reference input for POPUP system consisting in actuator, driver, and multi-body model, q, $\dot{q}$ and $\ddot{q}$ are the motor joint position, velocity and acceleration respectively.

Results are shown in Figure 12, where trajectories of RBM and PRBM are compared. Since the control algorithm uses RBM direct kinematics to calculate the EE position x_e, the equivalent robot with rigid link reaches correctly the target. Using PRBM, the trajectory is influenced by link deformations, as expected. In Figure 13 the absolute difference of EE position between RBM and PRBM during the task is shown.

The PRBM shows an error that depends on the configuration and payload, due to gravity that bends the links. A difference of 6.6 mm for the EE position is exhibited in the starting configuration, corresponding to joint variables q_0. The difference grows during the task up to 24.4 mm when the target is reached, since the final robot configuration is more extended, intensifying the deflections caused by payload.

The positioning error can be reduced with different strategies, as estimating the EE position with PRBM recurring to link sensor data. However this estimate depends on sensor accuracy, data fusion technique and simplification due to the adopted model.

Second simulation aims to validate a control strategy based on visual servoing (VS), with a camera mounted on the EE of the virtual robot with flexible link. Block scheme of robot control is shown in Figure 14.

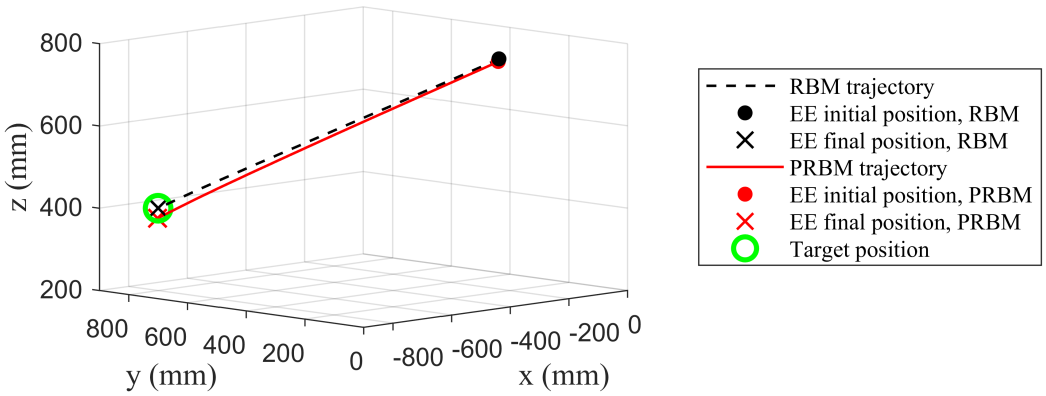

Figure 12. Trajectory of PRBM compared to RBM reaching the target using RBM-based control.

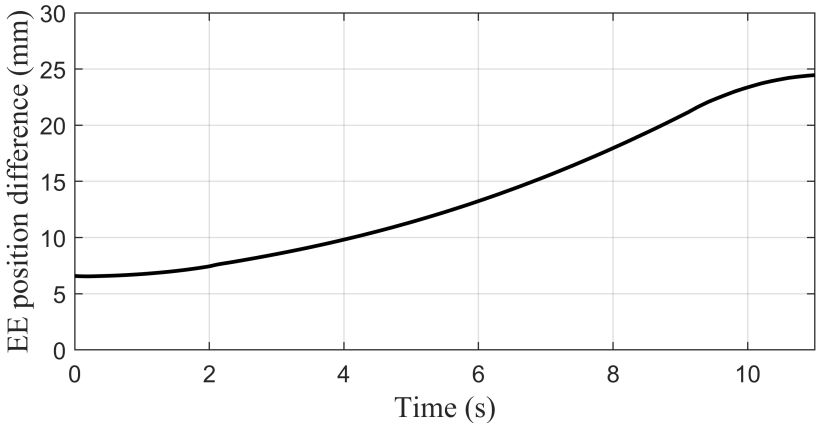

Figure 13. EE position difference of PRBM with respect to RBM during the task.

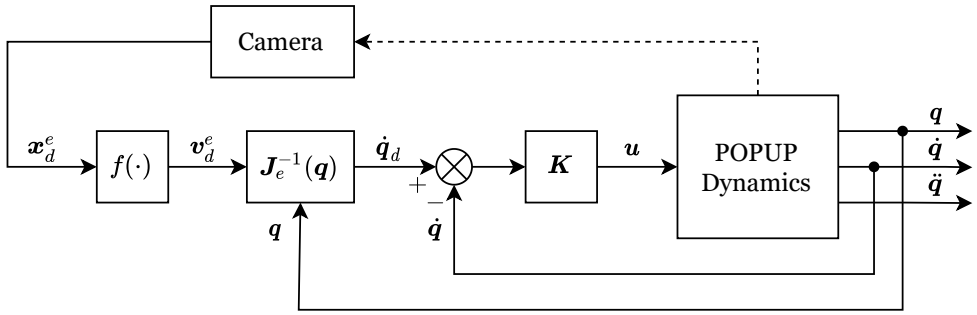

Figure 14. Block scheme of POPUP control using VS with camera mounted on EE.

Using computer vision algorithms, the camera can identify the target position in EE frame x_d^e. Then, the desired velocity in EE frame v_d^e is calculated by Equation (3), known $x_e^e = \mathbf{0}$. Finally, using Jacobian matrix of RBM in EE frame $J_e(q)$, the desired joint velocity $\dot{q}_d$ is calculated. Simulation provides exact feedback for target position x_d^e, validating the control algorithm independently from vision system errors.

Results are shown in Figure 15. The robot with flexible links using PRBM, on which camera is virtually positioned, correctly reaches the target, demonstrating how this strategy is able to compensate link deflections minimizing the positioning error between target and EE. Trajectories calculated using PRBM and RBM with same joint state are plotted, underlining the difference in positioning between the virtual robot with flexible links and an equivalent robot with rigid links. With reference to Figure 8, since Jacobian matrix of RBM is used, EE_{RBM} frame is evaluated as actual EE frame. On the other hand, measured target position x_d^e is referred to EE_{PRBM} frame. Nonetheless, the control algorithm effectively compensates errors due to small deflections.

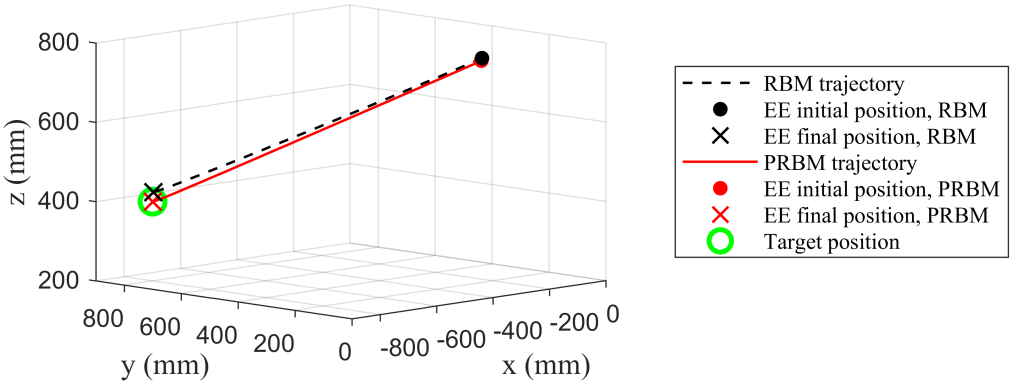

Figure 15. Trajectory of PRBM compared to RBM reaching the target using VS.

In Figure 16 motor joint position values $\boldsymbol{q}$ are shown during the task, highlighting corrections provided by the camera-based algorithm with respect to a traditional robot control in order to precisely reach the target.

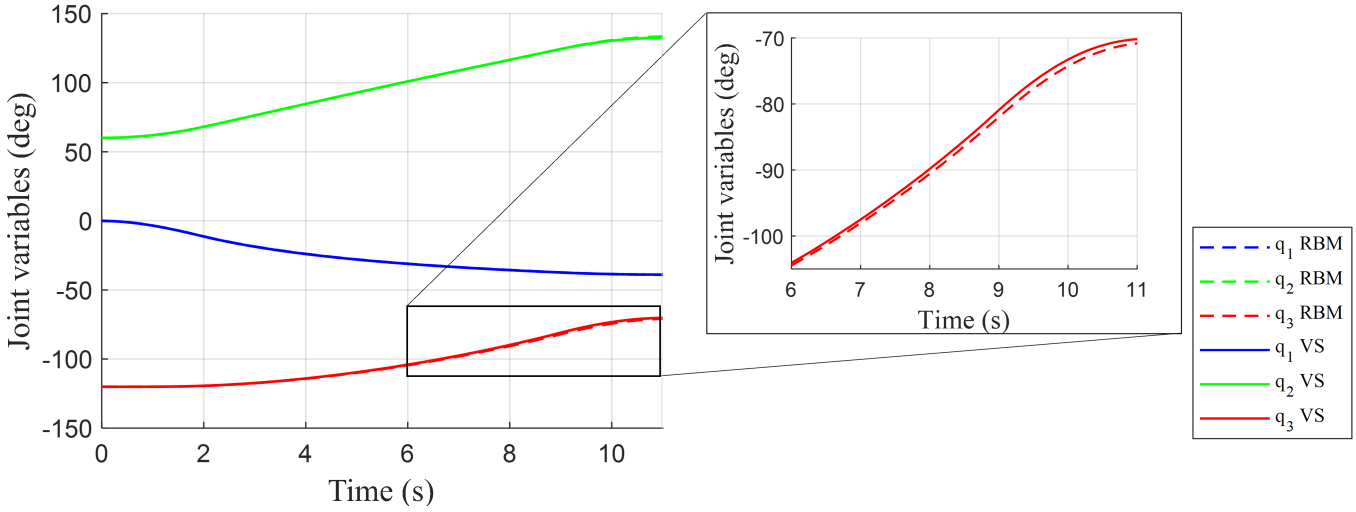

Figure 16. Motor joint position during the two simulations with RBM-based and VS control.

Results demonstrate the effectiveness of the presented control strategy based on visual servoing. Moreover, the algorithm potentially allows us to follow a target in movement. Since the desired position is correctly reached in the simulated environment providing exact feedback, the accuracy in positioning of POPUP depends on computer vision algorithms that have to be developed.

6. Conclusions

The prototype of POPUP, a deployable and inflatable robotic arm, has been proposed. The robot consists of two inflatable link and three rigid revolute joints actuated by electric motors. It can be stored in a relatively small box and deployed when required by inflation. The robot prototype has been described, underlining the design criteria and performance in terms of achievable payloads, in relation to the internal pressure. System architecture has been explained, focusing on sensors, electronics and pneumatic line, and proposing a control strategy based on sensor fusion techniques. A demonstration of deployment stage has been performed to highlight the packing ratio of the robotic arm prototype.

A pseudo-rigid body model has been used to describe the inflatable link behavior. Experimental tests has been performed to analyze the static and dynamic performance of the link, on varying the internal pressure. Results confirm the benefit of using wrinkling moment formula as design criteria, and validate the approximation of a linear static

characteristics for loads under the wrinkling condition. However, the presence of hysteresis produces uncertainties on link characterization.

The robot kinematics has been modified introducing virtual joint variables and a multi-body model has been developed, according to experimental tests. Simulations have been performed to highlight differences in terms of positioning with a rigid link robot. Moreover, a control algorithm based on vision servoing, has been validated showing how errors due to link deflections can be compensated using a camera mounted on the end-effector.

Results suggest that link deflection and hysteresis are phenomena to be taken into account for development of robot control algorithms. The use of IMUs or generic accelerometers could allow the control law to reduce maximal accelerations and avoid wrinkling. The use of multiple sensors on robot links, as flex sensors and IMUs, could lead to the development of a better estimate of the link state and consequently of the robot state, monitoring the distance from theoretical wrinkling area and guaranteeing better performances.

Further works will focus on the implementation and validation of proposed control algorithm on the robot prototype. A comparison with models based on finite-element approach will be executed. The estimation of robot accuracy and precision will be carry out in relation to different sensor equipment. Control algorithms have to be improved including dynamic tuning of maximal acceleration, accounting link deflection state, defining a suitable state machine to manage the robot and developing computer vision algorithms for target identification and following.

Author Contributions: Conceptualization, P.P., M.M. and S.M.; methodology, P.P., M.M. and S.M.; software, P.P. and M.M.; validation, P.P., M.M. and S.M.; formal analysis, P.P., M.M. and S.M.; investigation, P.P. and M.M.; resources, S.M.; data curation, P.P., M.M. and S.M.; writing—original draft preparation, P.P. and M.M.; writing—review and editing, P.P., M.M. and S.M.; visualization, P.P., M.M. and S.M.; supervision, S.M.; project administration, S.M.; funding acquisition, S.M. All authors have read and agreed to the published version of the manuscript.

Funding: This research received no external funding.

Institutional Review Board Statement: Not applicable.

Informed Consent Statement: Not applicable.

Data Availability Statement: Not applicable.

Acknowledgments: Authors thank Massimiliano Corrado Mattone for providing technical support in the experiments.

Conflicts of Interest: The authors declare no conflict of interest.

Abbreviations

The following abbreviations are used in this manuscript:

IAE	Inflatable Antenna Experiment
IRA	Inflatable robotic arm
PAM	Pneumatic artificial muscle
MPC	Model predictive control
LQR	Linear quadratic regulation
SMC	Sliding mode control
HRC	Human-robot collaboration
AMM	Assumed mode method
FEM	Finite element method
DOF	Degrees of freedom
MMOD	Micrometeoroids and orbital debris
EE	End-effector
RV	Reducing valve
PT	Pressure transducer

IMU	Inertial measurement unit
PRBM	Pseudo-rigid body model
RBM	Rigid body model
PSD	Power spectral density
FRF	Frequency response function
D-H	Denavit-Hartenberg
VS	Visual servoing

References

1. Chen, F.; Wang, M.Y. Design optimization of soft robots: A review of the state of the art. *IEEE Robot. Autom. Mag.* **2020**, *27*, 27–43. [CrossRef]
2. Laschi, C.; Mazzolai, B.; Cianchetti, M. Soft robotics: Technologies and systems pushing the boundaries of robot abilities. *Sci. Robot.* **2016**, *1*, eaah3690. [CrossRef] [PubMed]
3. Methenitis, G.; Hennes, D.; Izzo, D.; Visser, A. Novelty search for soft robotic space exploration. In Proceedings of the 2015 Annual Conference on Genetic and Evolutionary Computation, Madrid, Spain, 11–15 July 2015; pp. 193–200.
4. Qi, R.; Khajepour, A.; Melek, W.W.; Lam, T.L.; Xu, Y. Design, kinematics, and control of a multijoint soft inflatable arm for human-safe interaction. *IEEE Trans. Robot.* **2017**, *33*, 594–609. [CrossRef]
5. Hofer, M.; D'Andrea, R. Design, fabrication, modeling and control of a fabric-based spherical robotic arm. *Mechatronics* **2020**, *68*, 102369. [CrossRef]
6. Ataka, A.; Abrar, T.; Putzu, F.; Godaba, H.; Althoefer, K. Model-based pose control of inflatable eversion robot with variable stiffness. *IEEE Robot. Autom. Lett.* **2020**, *5*, 3398–3405. [CrossRef]
7. Kim, S.; Laschi, C.; Trimmer, B. Soft robotics: A bioinspired evolution in robotics. *Trends Biotechnol.* **2013**, *31*, 287–294. [CrossRef]
8. Yamaguchi, D.; Hanaki, T.; Ishino, Y.; Takasaki, M.; Mizuno, T. Fabrication of a Polyimide Film Pneumatic Actuator by Molding and Welding Processes. *Actuators* **2021**, *10*, 177. [CrossRef]
9. Hughes, J.; Culha, U.; Giardina, F.; Guenther, F.; Rosendo, A.; Iida, F. Soft manipulators and grippers: A review. *Front. Robot. AI* **2016**, *3*, 69. [CrossRef]
10. Oliveira, J.; Ferreira, A.; Reis, J.C. Design and experiments on an inflatable link robot with a built-in vision sensor. *Mechatronics* **2020**, *65*, 102305. [CrossRef]
11. Gillespie, M.T.; Best, C.M.; Killpack, M.D. Simultaneous position and stiffness control for an inflatable soft robot. In Proceedings of the 2016 IEEE International Conference on Robotics and Automation (ICRA), Stockholm, Sweden, 16–21 May 2016; pp. 1095–1101.
12. Diftler, M.; Ahlstrom, T.; Ambrose, R.; Radford, N.; Joyce, C.; De La Pena, N.; Parsons, A.; Noblitt, A. Robonaut 2—Initial activities on-board the ISS. In Proceedings of the 2012 IEEE Aerospace Conference, Big Sky, MT, USA, 3–10 March 2012; pp. 1–12.
13. Schenker, P.S. Advances in rover technology for space exploration. In Proceedings of the 2006 IEEE Aerospace Conference, Big Sky, MT, USA, 4–11 March 2006; p. 23.
14. Sujan, V.A.; Dubowsky, S. Design of a lightweight hyper-redundant deployable binary manipulator. *J. Mech. Des.* **2004**, *126*, 29–39. [CrossRef]
15. Cadogan, D.; Stein, J.; Grahne, M. Inflatable composite habitat structures for lunar and mars exploration. *Acta Astronaut.* **1999**, *44*, 399–406. [CrossRef]
16. Freeland, R.; Bilyeu, G.; Veal, G.; Steiner, M.; Carson, D. Large inflatable deployable antenna flight experiment results. *Acta Astronaut.* **1997**, *41*, 267–277. [CrossRef]
17. Malone, P.K.; Williams, G.T. Lightweight inflatable solar array. *J. Propuls. Power* **1996**, *12*, 866–872. [CrossRef]
18. Chandra, A.; Thangavelautham, J. Modular inflatable composites for space telescopes. In Proceedings of the 2019 IEEE Aerospace Conference, Big Sky, MT, USA, 2–9 March 2019; pp. 1–9.
19. Webster, R.J., III; Jones, B.A. Design and kinematic modeling of constant curvature continuum robots: A review. *Int. J. Robot. Res.* **2010**, *29*, 1661–1683. [CrossRef]
20. Chirikjian, G.; Burdick, J. The kinematics of hyper-redundant robot locomotion. *IEEE Trans. Robot. Autom.* **1995**, *11*, 781–793. [CrossRef]
21. De Luca, A.; Book, W.J. Robots with flexible elements. In *Springer Handbook of Robotics*; Springer: Berlin/Heidelberg, Germany, 2016; pp. 243–282.
22. Sanan, S.; Moidel, J.B.; Atkeson, C.G. Robots with inflatable links. In Proceedings of the 2009 IEEE/RSJ International Conference on Intelligent Robots and Systems, St. Louis, MO, USA, 10–15 October 2009; pp. 4331–4336.
23. Raviola, A.; Martin, A.D.; Guida, R.; Pastorelli, S.; Mauro, S.; Sorli, M. Identification of a UR5 Collaborative Robot Dynamic Parameters. In Proceedings of the International Conference on Robotics in Alpe-Adria Danube Region, Poitiers, France, 21–23 June 2021; pp. 69–77.
24. Raviola, A.; Guida, R.; De Martin, A.; Pastorelli, S.; Mauro, S.; Sorli, M. Effects of temperature and mounting configuration on the dynamic parameters identification of industrial robots. *Robotics* **2021**, *10*, 83. [CrossRef]
25. Li, X.; Sun, K.; Guo, C.; Liu, T.; Liu, H. Design, modeling and characterization of a joint for inflatable robotic arms. *Mechatronics* **2020**, *65*, 102311. [CrossRef]

26. Best, C.M.; Wilson, J.P.; Killpack, M.D. Control of a pneumatically actuated, fully inflatable, fabric-based, humanoid robot. In Proceedings of the 2015 IEEE-RAS 15th International Conference on Humanoid Robots (Humanoids), Seoul, Korea, 3–5 November 2015; pp. 1133–1140.
27. Best, C.M.; Rupert, L.; Killpack, M.D. Comparing model-based control methods for simultaneous stiffness and position control of inflatable soft robots. *Int. J. Robot. Res.* **2021**, *40*, 470–493. [CrossRef]
28. Mattiazzo, G.; Mauro, S.; Raparelli, T.; Velardocchia, M. Control of a six-axis pneumatic robot. *J. Robot. Syst.* **2002**, *19*, 363–378. [CrossRef]
29. Giorelli, M.; Renda, F.; Calisti, M.; Arienti, A.; Ferri, G.; Laschi, C. Neural Network and Jacobian Method for Solving the Inverse Statics of a Cable-Driven Soft Arm with Nonconstant Curvature. *IEEE Trans. Robot.* **2015**, *31*, 823–834. [CrossRef]
30. Machkour, Z.; Ortiz-Arroyo, D.; Durdevic, P. Classical and Deep Learning based Visual Servoing Systems: A Survey on State of the Art. *J. Intell. Robot. Syst.* **2022**, *104*, 11. [CrossRef]
31. Xu, F.; Wang, H.; Chen, W.; Miao, Y. Visual Servoing of a Cable-Driven Soft Robot Manipulator With Shape Feature. *IEEE Robot. Autom. Lett.* **2021**, *6*, 4281–4288. [CrossRef]
32. Fang, G.; Wang, X.; Wang, K.; Lee, K.H.; Ho, J.D.L.; Fu, H.C.; Fu, D.K.C.; Kwok, K.W. Vision-Based Online Learning Kinematic Control for Soft Robots Using Local Gaussian Process Regression. *IEEE Robot. Autom. Lett.* **2019**, *4*, 1194–1201. [CrossRef]
33. Kunkelmoor, J.; Mercorelli, P. Design of a Real Time Path of Motion Using a Sliding Mode Control with a Switching Surface. In *Advanced, Contemporary Control*; Springer International Publishing: Cham, Switzerland, 2020; pp. 197–206.
34. Scimmi, L.S.; Melchiorre, M.; Mauro, S.; Pastorelli, S.P. Implementing a vision-based collision avoidance algorithm on a UR3 Robot. In Proceedings of the 2019 23rd International Conference on Mechatronics Technology (ICMT), Salerno, Italy, 23–26 October 2019; pp. 1–6.
35. Mauro, S.; Pastorelli, S.; Scimmi, L.S. Collision Avoidance Algorithm for Collaborative Robotics. *Int. J. Autom. Technol.* **2017**, *11*, 481–489. [CrossRef]
36. Palmieri, P.; Melchiorre, M.; Scimmi, L.S.; Pastorelli, S.; Mauro, S. Human Arm Motion Tracking by Kinect Sensor Using Kalman Filter for Collaborative Robotics. *Mech. Mach. Sci.* **2021**, *91*, 326–334.
37. Scimmi, L.S.; Melchiorre, M.; Mauro, S.; Pastorelli, S. Multiple Collision Avoidance between Human Limbs and Robot Links Algorithm in Collaborative Tasks. In Proceedings of the ICINCO (2), Porto, Portugal, 29–31 July 2018; pp. 301–308.
38. Melchiorre, M.; Scimmi, L.S.; Pastorelli, S.P.; Mauro, S. Collison avoidance using point cloud data fusion from multiple depth sensors: A practical approach. In Proceedings of the 2019 23rd International Conference on Mechatronics Technology (ICMT), Salerno, Italy, 23–26 October 2019; pp. 1–6.
39. Scimmi, L.S.; Melchiorre, M.; Troise, M.; Mauro, S.; Pastorelli, S. A practical and effective layout for a safe human-robot collaborative assembly task. *Appl. Sci.* **2021**, *11*, 1763. [CrossRef]
40. Sanan, S.; Ornstein, M.H.; Atkeson, C.G. Physical human interaction for an inflatable manipulator. In Proceedings of the 2011 Annual International Conference of the IEEE Engineering in Medicine and Biology Society, Boston, MA, USA, 30 August–3 September 2011; pp. 7401–7404.
41. Pang, G.; Deng, J.; Wang, F.; Zhang, J.; Pang, Z.; Yang, G. Development of Flexible Robot Skin for Safe and Natural Human–Robot Collaboration. *Micromachines* **2018**, *9*, 576. [CrossRef]
42. Jørgensen, J.; Bojesen, K.B.; Jochum, E. Is a Soft Robot More "Natural"? Exploring the Perception of Soft Robotics in Human–Robot Interaction. *Int. J. Soc. Robot.* **2022**, *14*, 95–113. [CrossRef]
43. Troise, M.; Gaidano, M.; Palmieri, P.; Mauro, S. Preliminary Analysis of a Lightweight and Deployable Soft Robot for Space Applications. *Appl. Sci.* **2021**, *11*, 2558. [CrossRef]
44. Palmieri, P.; Gaidano, M.; Troise, M.; Salamina, L.; Ruggeri, A.; Mauro, S. A deployable and inflatable robotic arm concept for aerospace applications. In Proceedings of the IEEE International Workshop on Metrology for AeroSpace, MetroAeroSpace 2021, Naples, Italy, 23–25 June 2021; pp. 453–458.
45. Palmieri, P.; Gaidano, M.; Ruggeri, A.; Salamina, L.; Troise, M.; Mauro, S. An Inflatable Robotic Assistant for Onboard Applications. In Proceedings of the International Astronautical Congress, IAC, Dubai, United Arab Emirates, 25–29 October 2021; Volume A5, pp. 25–29.
46. Chu, A.M.; Nguyen, C.D.; Duong, X.B.; Nguyen, A.V.; Nguyen, T.A.; Le, C.H.; Packianather, M. A novel mathematical approach for finite element formulation of flexible robot dynamics. *Mech. Based Des. Struct. Mach.* **2020**, 1–21. [CrossRef]
47. Aikenhead, B.A.; Daniell, R.G.; Davis, F.M. Canadarm and the space shuttle. *J. Vac. Sci. Technol. A* **1983**, *1*, 126–132. [CrossRef]
48. Veldman, S.L. *Design and Analysis Methodologies for Inflated Beams*; Delft University Press: Delft, The Netherlands, 2005.
49. Wielgosz, C.; Thomas, J.C. Deflections of inflatable fabric panels at high pressure. *Thin-Walled Struct.* **2002**, *40*, 523–536. [CrossRef]
50. Kalman, R. A new approach to linear filtering and prediction problems. *J. Basic Eng.* **1960**, *82*, 34–45. [CrossRef]